Effect of printing parameters on interlayer bond strength of 3D printed limestone-calcined clay-based cementitious materials

An experimental and numerical study

Chen, Yu; Jansen, Koen; Zhang, Hongzhi; Romero Rodriguez, Claudia; Gan, Yidong; Çopuroğlu, Oğuzhan; Schlangen, Erik

DOI
10.1016/j.conbuildmat.2020.120094

Publication date
2020

Document Version
Final published version

Published in
Construction and Building Materials

Citation (APA)
Chen, Y., Jansen, K., Zhang, H., Romero Rodriguez, C., Gan, Y., Çopuroğlu, O., & Schlangen, E. (2020). Effect of printing parameters on interlayer bond strength of 3D printed limestone-calcined clay-based cementitious materials: An experimental and numerical study. *Construction and Building Materials*, *262*, Article 120094. https://doi.org/10.1016/j.conbuildmat.2020.120094

Construction and Building Materials 262 (2020) 120094

Contents lists available at ScienceDirect

Construction and Building Materials

journal homepage: www.elsevier.com/locate/conbuildmat

Effect of printing parameters on interlayer bond strength of 3D printed limestone-calcined clay-based cementitious materials: An experimental and numerical study

Yu Chen [a], Koen Jansen [a], Hongzhi Zhang [a,b,*], Claudia Romero Rodriguez [a], Yidong Gan [a], Oğuzhan Çopuroğlu [a], Erik Schlangen [a]

[a] Microlab, Faculty of Civil Engineering and Geosciences, Delft University of Technology, Delft, The Netherlands
[b] School of Qilu Transportation, Shandong University, Jinan, PR China

HIGHLIGHTS

- The effect of different printing parameters on bond strength was investigated.
- Bond strength of printed limestone-calcined clay-cementitious materials was tested.
- The air void content and distribution of the printed specimens were analyzed.
- Bond strength of printed specimens can be predicted by a 2D lattice model.

ARTICLE INFO

Article history:
Received 21 March 2020
Received in revised form 16 June 2020
Accepted 25 June 2020

Keywords:
3D Concrete Printing
Interlayer Bond Strength
Air Void Content and Distribution
Lattice Fracture Model

ABSTRACT

For a single batch material, time intervals and nozzle standoff distances between two subsequent layers are two critical printing parameters that influence the mechanical performance of the printed concrete. This paper presents an experimental and numerical study to investigate the impacts of these printing parameters on the interlayer bond strength of the 3D printed limestone and calcined clay-based cementitious materials. All samples were manufactured by a lab-scale 3D printer equipped with a hybrid back- and down-flow nozzle (rectangular opening). The uniaxial tensile test was employed to quantify the interface adhesion of printed specimens. Moreover, the greyscale value image of microstructure, as well as the air void content and distribution of the printed specimens were acquired by X-ray computed tomography and characterized by image analysis. The experimental results showed that extending the time interval between construction of two layers could decrease the bond strength, whereas only increasing the nozzle standoff distance exhibited limited effects on that. The weak bond strength could be attributed to the high local porosity at the interface of the specimen. Additionally, numerical simulations of the uniaxial tensile test were conducted using a 2D lattice fracture model, which can predict the bond strength of printed specimens for different void content in the interface layer.

1. Introduction

In the past decade, extrusion-based 3D concrete printing (3DCP) as an emerging construction technology has attracted remarkable attention from both academia and industry worldwide [1–3]. The working mechanism of 3DCP could be understood as linear filaments of cementitious materials being extruded and deposited layer by layer to form objects without the aid of formwork [4]. As reported by many studies [5–9,63], 3DCP could bring many benefits to concrete construction, e.g., increasing flexibility of architectural design, eliminating formwork, reducing wastes, and saving labor costs. In comparison with conventional concrete, the fresh cementitious materials for 3DCP were required to exhibit many specific rheological properties, including extrudability, and buildability during the printing process.

To satisfy these rheological requirements, aggregate content is reduced [10,11], which leads to an increased quantity of binder in the mix design of printable cementitious materials [3]. Until today, most of the proposed mix designs for 3DCP contained a high volume of ordinary Portland cement (OPC) [2,3,12,13]. The

* Corresponding author at: School of Qilu Transportation, Shandong University, 250002 Jinan, PR China.
E-mail addresses: Y.Chen-6@tudelft.nl (Y. Chen), hzzhang@sdu.edu.cn (H. Zhang).

https://doi.org/10.1016/j.conbuildmat.2020.120094
0950-0618/

Table 1
Mix design of 3D printable cementitious material (wt.% of the binder mass).

Type	PC	Calcined Clay		LP	Sand	Water	SP	VMA
		Low-grade	High-grade					
Content (wt.%)	40	30	10	20	150	30	2	0.24

production of OPC leads to many negative impacts on the environment, such as non-negligible CO_2 emissions and large amounts of energy consumption. Replacing high volumes of OPC by supplementary cementitious materials (SCMs) is gradually becoming a solution for developing sustainable mixtures for 3DCP [2,12]. However, as mentioned by Scrivener [14], the main problem of using common SCMs, including fly ash, slag, and silica fume, is the limited supplies. Calcined clay as an alternative source of SCMs is widely available and has been utilized in concrete. The limestone and calcined clay cement (LC3), containing only 50% of the clinker in the binder composition, has been developed and produced successfully in Cuba and India [14–16]. The advantages of using LC3 in concrete have been reported by many researchers [17–20], e.g., low CO_2 emissions, comparable mechanical performance with plain OPC after 7 days, and good resistance to chemical attacks. It is also feasible to use limestone and calcined clay to substitute high volumes of OPC in the printable cementitious materials [3,13]. Alternative mix designs and fresh state behaviors of limestone and calcined clay-based printable cementitious materials have been reported in our previous studies [2,8,21–23]. Nevertheless, to our knowledge, currently no dedicated study reported the mechanical performance of 3D printed limestone and calcined clay-based cementitious materials.

The interlayer bond strength, also known as interlayer strength or bond strength, between two adjacent layers is believed to be a weakness in a printed structure [24]. The cold joint is usually referred to as the weak interlayer adhesion due to a lack of intermixing between the old and new layers [25–27]. From the material

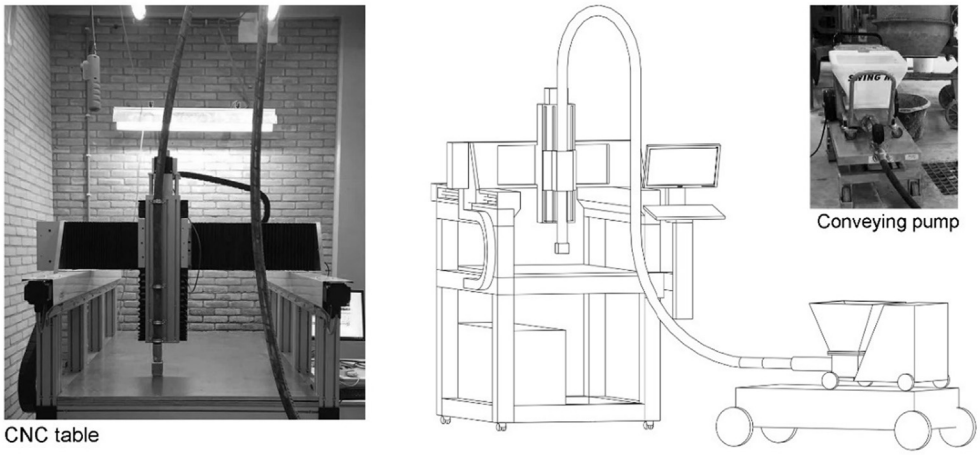

(a)

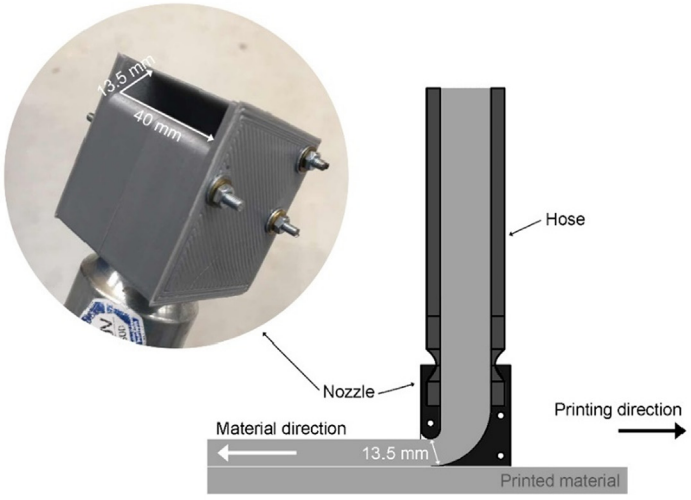

(b)

Fig. 1. (a) A lab-scale extrusion-based 3DCP setup at TU Delft. (b) Schematic section of the hybrid back- and down-flow nozzle.

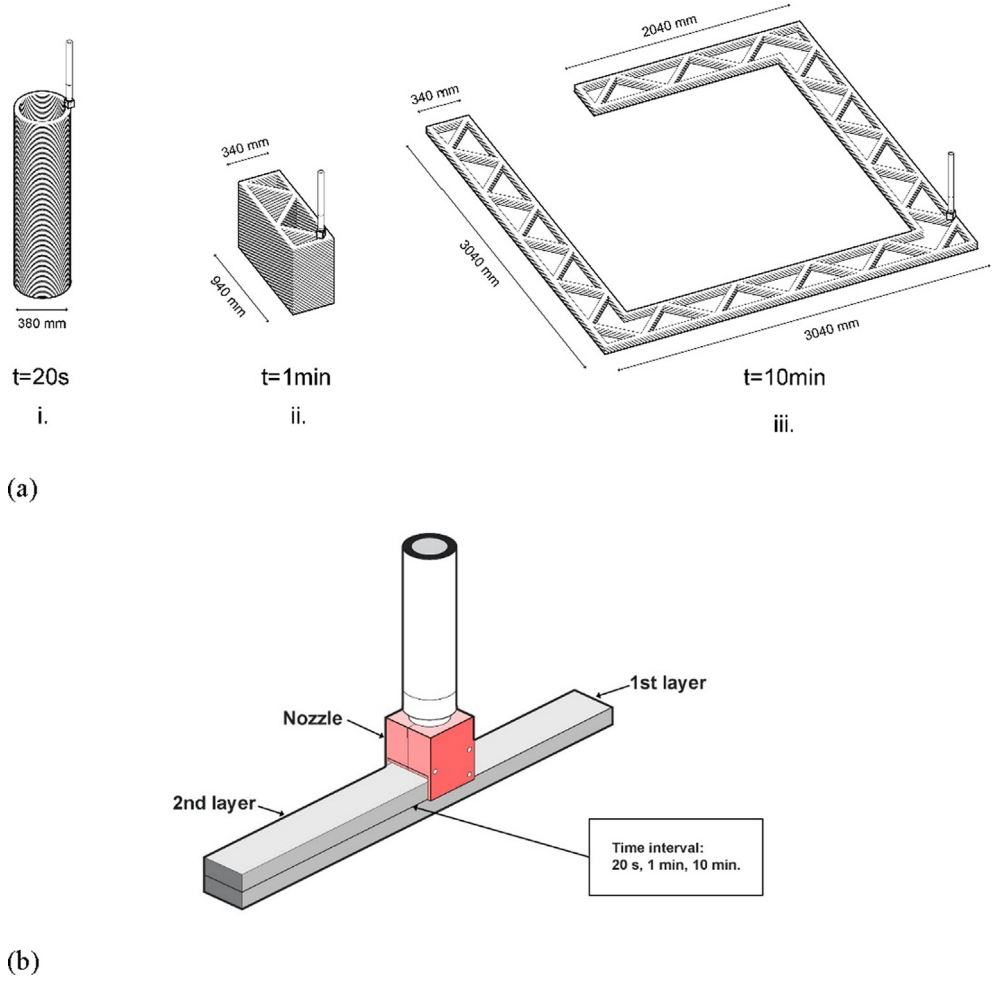

Fig. 2. (a) Three scenarios: i. a small object with 1200 mm of path length for each layer (Time interval-20 s); ii. a medium object with 3600 mm of path length for each layer (Time interval-1 min); and iii. a large object with 36000 mm of path length for each layer (Time interval-10 min). (b) Schematic diagram of the printing process by different time intervals between two layers.

aspect, thixotropy plays a dominant role in forming cold joints [26]. In 3DCP, a high thixotropy (or structuration rate) of fresh cementitious materials is required to ensure that the deposited layers have sufficient yield stress to sustain the gravity-induced dead weight of the gradually increasing layers [24]. However, materials with a high thixotropy could easily lead to a weak interface adhesion [26,28]. This phenomenon has been initially observed in self-compacting concrete [25,29] and was confirmed by several recent studies about printable cementitious materials [27,30]. Besides thixotropy, the bond strength may also be influenced by two printing parameters as follows:

(1) *The time interval between two subsequent layers*. According to many earlier studies [4,9,26,30–32], extending the time gap between layers could provide sufficient time for the static yield stress evolution of the deposited layers to enhance the buildability, whereas it would decrease the bond strength. The time interval could be as short as several seconds (minutes) or could be longer than 10 h. Since cement is a time-dependent material, the printability window may be a boundary to divide the short and long-time intervals. For short-time intervals (within the printability window), the material of both layers is from the same batch (Note that, the process like continuous mixing/production of fresh mixtures is not considered in this study. In this case, multiple small batches were employed within a short period.). Tay et al. [31] provided a good example for determining the tensile bond strength between two layers with short-time intervals ranging from 1 min to 20 min by using a direct tensile test. A strong correlation between the time-dependent rheological behavior and interface adhesion has been observed. Their study confirmed that the thixotropy of the deposited material has a severe impact on the adhesion at the interface between two layers for short-time intervals.
In addition, many studies [4,9,32] also targeted the investigation towards the effects of long-time intervals (after the printability window) on the bond strength. In this situation, the mixtures of the first and second layers were not prepared at the same time. The printing environment may play a dominant role in influencing bond strength. The experimental results in [4,33,34] showed that the exposed resting layer under a drying environment could lead to a considerable reduction in bond strength while protecting the layer from drying was an efficient way to improve the bond strength for long-time intervals. Sanjayan et al. [35] and Van Der Putten et al. [36] pointed out that the moisture content of the layer surface is of significant importance regarding the tensile bond strength. Therefore, for long-time intervals, the task should be shifted to seeking better methods to maintain the surface moisture of the deposited layers.

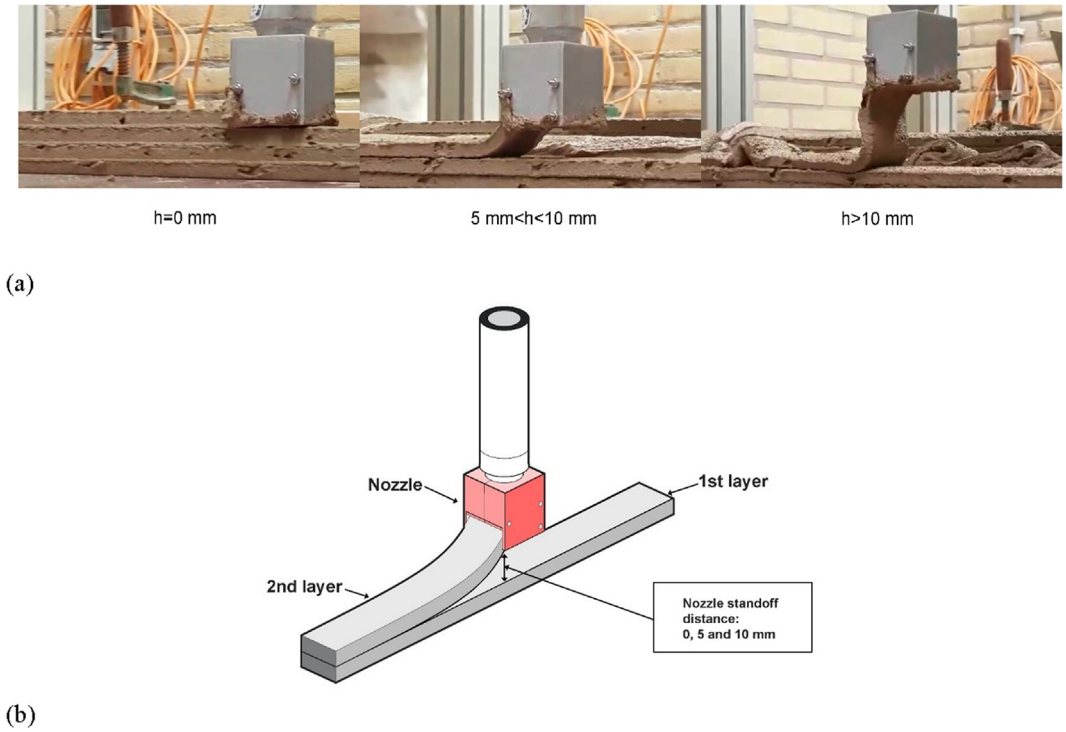

Fig. 3. (a) Increasing the nozzle standoff distance *h* could lead to the inaccurate layer deposition; (b) Schematic diagram of the printing process by different nozzle standoff distances between two layers.

(2) *The nozzle standoff distance*. The material deformation could hardly be avoided during a printing process. The height change of deposited layers would vary the nozzle standoff distance that might influence the interlayer bond strength. Panda et al. [9] found a severe decrease in more than 30% of bond strength with increasing the nozzle standoff distance. However, limited effects have been found in the study of Wolfs et al. [4]. The authors reported that the deviation of results becomes more significant when increasing the nozzle height from the default setting. The different results may be attributed to the differences in mixture and nozzle type, for instance, shapes of opening (round or rectangle), directions of material deposition (back- or down-flow), and others. These variables of nozzles may influence the contact pressures and surface areas between two layers, which could affect the interlayer bonding. However, to our knowledge, the effect of different nozzle types on bond strength is still an opened research question.

For quasi-brittle materials, the increment of porosity could be one reason for the reduction of strength [37]. Panda et al.[30] and Tay et al. [31] reported that the macropore content in the interlayer affected the bond strength of printed cementitious materials. Macropores or air voids in the interfacial zone may be due to a lack of efficient contact areas between two layers. Through scanning electron microscope (SEM) observations, Nerella et al. [34] found large cavities between two layers for the sample with lower bond strength. Several methods were introduced to improve the bond strength between consecutive layers. Zareiyan and Khoshnevis [27] illustrated that increasing the effective contact areas between two layers through interlocking could contribute to improving the interlayer bond strength. A similar method was used by Van der Putten et al. [36]. The authors adopted a comb to make the rough surface and create the interlocking of the deposited layer, which also showed a positive result for enhancing the tensile bond strength. Besides, Marchment et al. [38] employed a paste layer on the substrate layer before the deposition of subsequent layer. The enhancement of bond strength was also evident.

Most of the recent studies attempted to explore the mechanism of interface formation induced by different printing parameters. Performing uniaxial tensile test [9,31,32,35,36,38] is a direct way to obtain the bond strength between two layers. However, for printed cementitious materials, the details of the uniaxial tensile tests are not so commonly reported in the literature, i.e., the complete load and displacement curve including pre- and post-peak properties. In general, there is a lack of knowledge regarding fracture mechanics and fracture modeling within the context of 3D printed cementitious materials.

Lattice fracture model, as a mechanical modeling approach, is widely used to explain the fracture behavior of cementitious materials since the simulated crack patterns and tensile strengths are very close to those observed in experiments [39,40]. Earlier studies [40–43] employed the discrete lattice fracture model to predict and model the fracture process of the digital specimen in a mechanical test, e.g., compression, flexural, splitting, and uniaxial tensile strength. The digital specimen, mimicking the cementitious material (the input of material mesostructure), can be constructed by using different techniques, e.g., X-ray computed tomography [42–44], nanoindentation [45], and others [46,47].

The printing parameters, including short-time intervals and nozzle standoff distances, seemed extremely critical for a single batch material in practice. This paper aims to investigate the effect of these printing parameters on the interlayer bond strength of 3D printed limestone-calcined clay-based cementitious materials. The printed specimens were tested in the uniaxial tension under a non-rotational boundary condition for obtaining the complete load and displacement curve (containing the softening branch). Furthermore, X-ray computed tomography scanning was used for acquiring the digital material structure. Based on the obtained digital material structure, the air void (also known as macropores) con-

tent and distribution were measured and analyzed as well. Finally, numerical simulations of the experiments were conducted using a 2D lattice fracture model.

2. Experimental program

2.1. Materials

A printable mixture proposed in our previous study [23] was used in this paper. As shown in Table 1, the binder was a ternary blend of CEM I 52.5R type Portland cement (PC), limestone powder (LP), and calcined clay. The calcined clay was prepared by mixing low- and high-grade calcined clay in a 3:1 proportion. Through using a chemical dissolution method [2], the reactive content of the low-grade calcined clay and the high-grade calcined clay was determined as 48.8 wt% and 75.1 wt%, respectively. Quartz sand with the maximum grain diameter of 2 mm was used as aggregate that possessed near 60% of the total mass of dry components. It is worth noting that the printable mixture used in this study should be called 3D printable mortar technically due to no coarse aggregate addition. The water to binder ratio was 0.3. Besides, 2% of the binder mass of polycarboxylate ether-based superplasticizer (SP) and 0.0024% of hydroxypropyl methylcellulose-based viscosity modifying admixture (VMA) were added in the mixture to adjust the fresh properties for printing.

For 3D printing, the fresh materials were prepared according to the following procedure:

(1) t = −4 min, homogenizing the dry materials (binder + sand) at speed 1 (60 rpm) by a HOBART planetary mixing machine.
(2) t = 0 min, adding water and superplasticizer, and keeping speed 1.
(3) t = 3.5 min, stopping, and adding VMA. Mixing at speed 1.
(4) t = 7 min, scraping the bottom and wall of the container.
(5) t = 7.5 min, mixing at speed 2 (124 rpm).
(6) t = 10 min, stopping, and casting/printing.

2.2. 3D concrete printing setup

The samples were printed by the 3DCP setup of Delft University of Technology (TU Delft), which has been introduced by [22,23]. As illustrated in Fig. 1 (a), there are two main parts of the printing system: an extrusion configuration (a nozzle, a material hose, and a PFT Swing M conveying pump) and a three-degree freedom Computer Numerical Control (CNC) table (length × width × height of the workspace: 1100 × 720 × 290 mm^3). Up to 38 L of the fresh mixture could be filled into the hopper of pump manually. Under the extrusion force, the fresh mixture was delivered from the hopper container through the hose (inner diameter: 25 mm; length: 5 m) to the nozzle. As suggested by Wolfs [48], a hybrid down- and back-flow nozzle was utilized in this study (Fig. 1 (b)). The nozzle with a rectangle-opening of 40 × 13.5 mm^2 could provide a large contact surface area between two layers, which may ensure printing stability. The moving speed of the nozzle was set as 60 mm/s with respect to a material flow rate of 1.9 L/min. Samples were printed and prepared under the same ambient condition of 20 ± 2 °C and about 55% RH.

2.3. Sample preparation

All printed objects with the designed dimensions of 800 mm in length, 25–27 mm in height, and 40 mm in width consisted of two layers (only one filament for each layer). Two printing parameters were investigated in this paper: the time interval between two adjacent layers, as well as the height between the bottom of the nozzle and the substrate (nozzle standoff distance).

2.3.1. Time interval

In this study, the default printing speed was 60 mm/s. Thus, assuming the object has the identical layers (the same path length of each layer) from the bottom to the top, 20 s, 1 min, and 10 min of time intervals may represent three scenarios in Fig. 2 (a): objects with path length of 1200 mm, 3600 mm, and 36000 mm for each layer, respectively. In this test series, the nozzle standoff distance was kept as 0 mm. The first layer was exposed to the ambient envi-

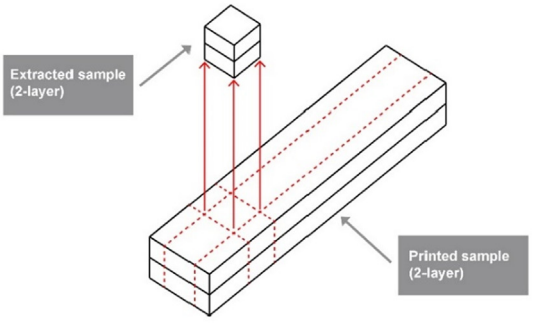

(a)

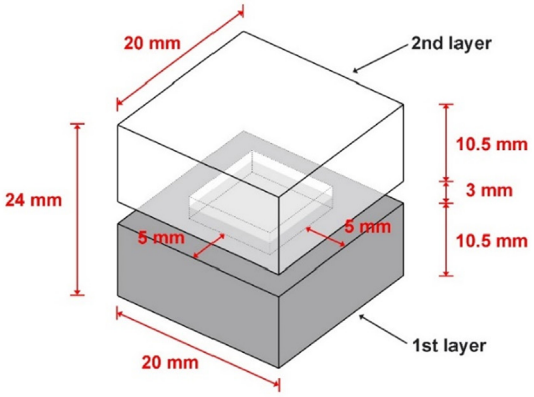

(b)

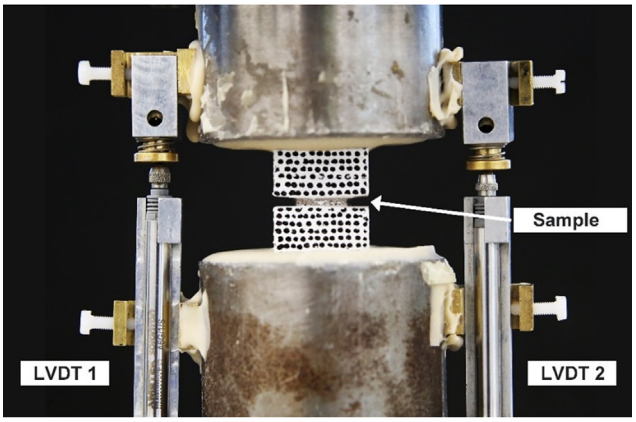

(c)

Fig. 4. (a) Extracting the specimen from the printed sample; (b) Illustration of the specimen for performing uniaxial tensile test; (c) A photograph of the uniaxial tensile test setup.

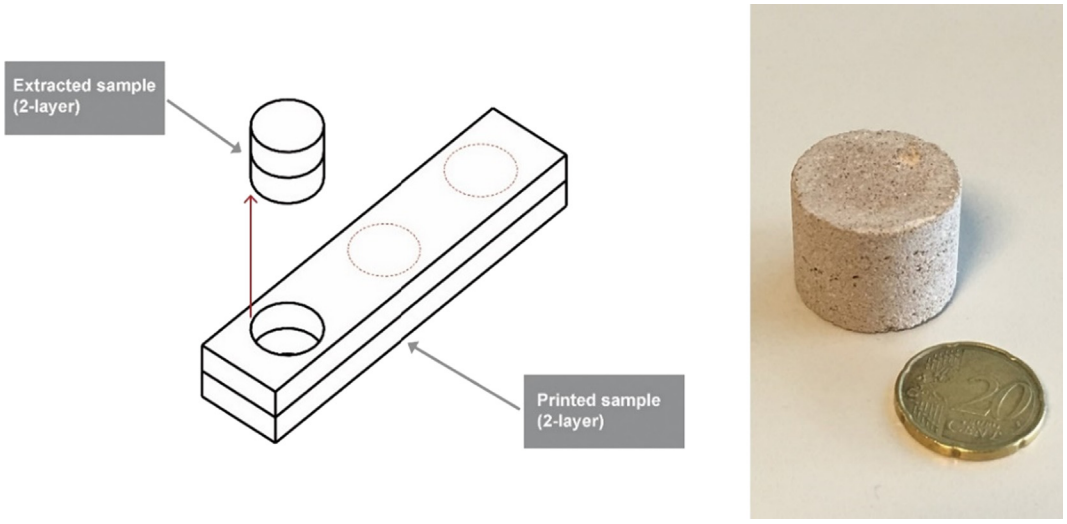

Fig. 5. Extracting specimens from the printed sample (left); A photograph of the cored specimen for XCT scanning (right).

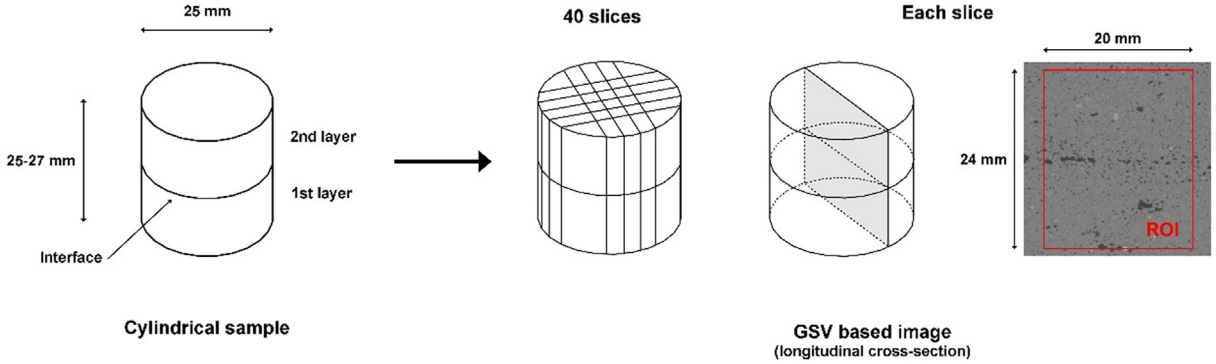

Fig. 6. The process of acquiring GSV based images for air void analysis and modeling.

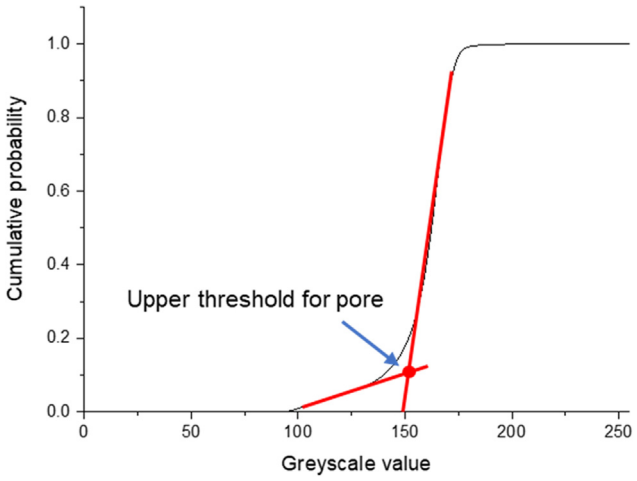

Fig. 7. Schematic explanation of the approach used to segment the air voids.

ronment without any cover, and the second layer was laid after a time interval of 20 s, 1 min, and 10 min, respectively (see Fig. 2 (b)).

2.3.2. Nozzle standoff distance

The nozzle was featured as a hybrid back- and down-flow (see Fig. 1 (b)). According to our preliminary printing tests (see Fig. 3 (a)), nozzle standoff distance greater than 10 mm led to inaccurate positioning of the layers. Therefore, as shown in Fig. 3 (b), three different nozzle standoff distances 0, 5, and 10 mm were selected to make the second layer. 0 mm was the default value, and 10 mm was the maximum tolerance value. For each trial, the time gap between the two adjacent layers was controlled as 1 min in this test series.

2.3.3. Mold-cast specimen

Cast samples with dimensions of 160 × 40 × 40 mm^3 were also prepared and tested. Fresh mixtures were filled into the mold manually. No compaction was applied. Both cast and printed samples were stored under the plastic film for the first 24 h. Afterwards, all samples were cured and stored in a fog room (20 ± 2 °C, and 99% RH) before conducting the tests.

2.4. Uniaxial tensile test

Uniaxial tensile test was performed to determine the bond strength of printed and cast samples. One day before testing, three specimens (Fig. 4 (a) (b)) with 20 mm of length, 20 mm of width, and 24 mm of height were sawn from the printed and mold-cast objects by using a cutting machine. To ensure the printed sample failed at the interface zone, a notch with a depth of 5 mm and a height of 3 mm was made on four sides of the sample at the interlayer (Fig. 4 (b)). The notches were also made on the cast samples at the same position. Uniaxial tensile tests were conducted on a servo-hydraulic Instron 8872 machine. Before implementing the

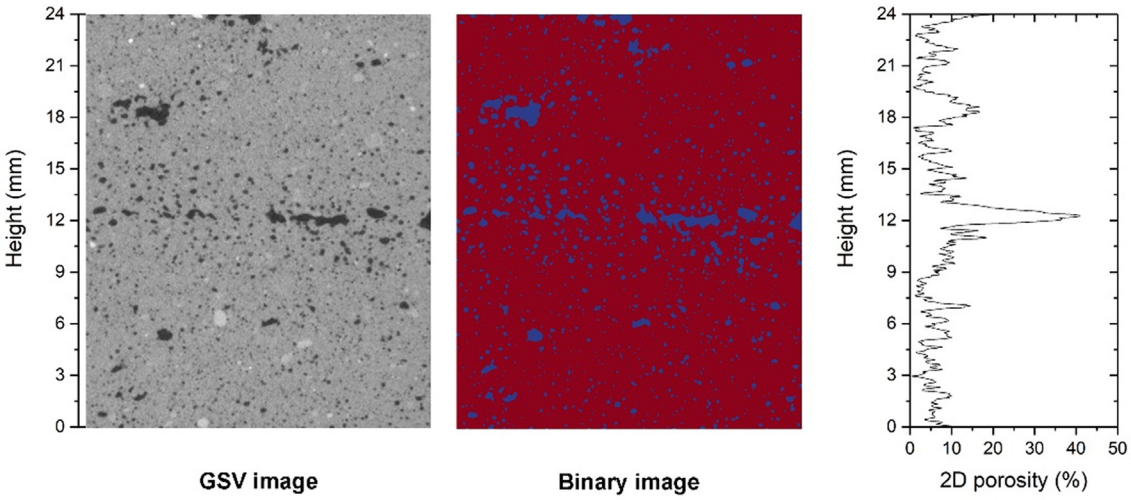

Fig. 8. GSV based XCT image (left); The segmented binary image (middle); The air void analysis of the binary image (right).

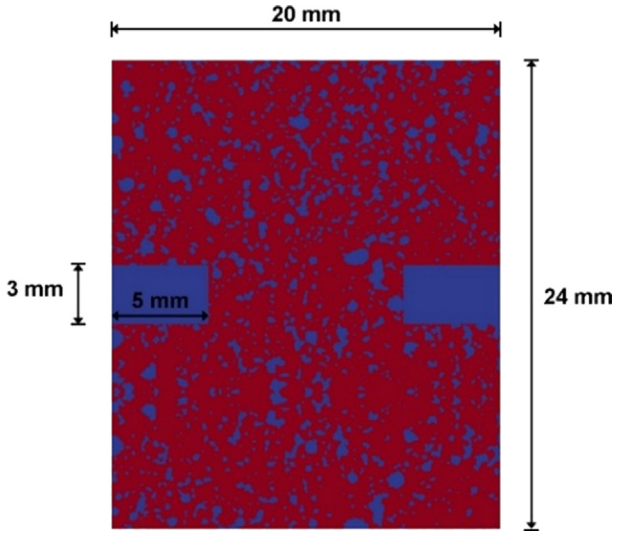

Fig. 9. The notched digital specimen (cast specimen) used for the fracture and deformation analysis.

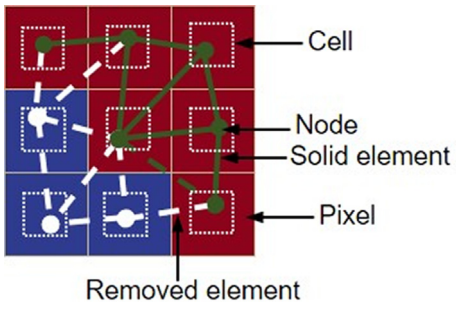

Fig. 10. Schematic illustration of the 2D mesh generation.

test, the frontal surface of specimens was painted white by using acrylic paint. Afterwards, evenly distributed black dots were randomly made with a permanent marker for employing digital image correlation (DIC). The prepared specimens were glued between two non-rotating platens via using a rapid hardening adhesive to keep the same deformation along the four sides of the specimen

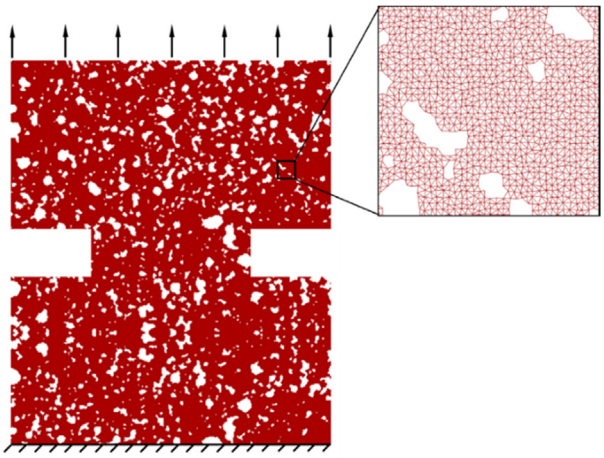

Fig. 11. The boundary condition of the computational uniaxial tension test.

(Fig. 4 (c)). The test was controlled by the average value of two linear variable differential transducers (LVDTs) at loading speed of 0.01 μm/s. A Canon camera model EOS 6D equipped with a Tamron aspherical 28–75 mm lens was utilized to acquire images during the test process. DIC of each test was analyzed by an open-source software Ncorr2 [49].

2.5. X-ray computed tomography

In this study, X-ray computed tomography (XCT) scanning was used to acquire the greyscale-based digital microstructure of the printed and cast specimens for air void analysis and specimen digitalization for modeling. In Fig. 5, cylindrical samples with a circular cross-section of 25 mm diameter and 25–27 mm height were drilled from both printed and cast objects (at the material age of 7 days), which were manufactured in Section 2.3. The prepared specimens were scanned by a Phoenix Nanotom Micro CT-Scanner. Under the setting of 120 kV/60 μA of the X-ray source, 1441 tomographic images were obtained on a digital GE DXR detector (3072 × 2400 pixel^2), and a spatial resolution of 50 × 50 × 50 μm^3/voxel was acquired. The 3D tomographic reconstruction was carried out with the software Phoenix Datos|x Reconstruction 2.0.

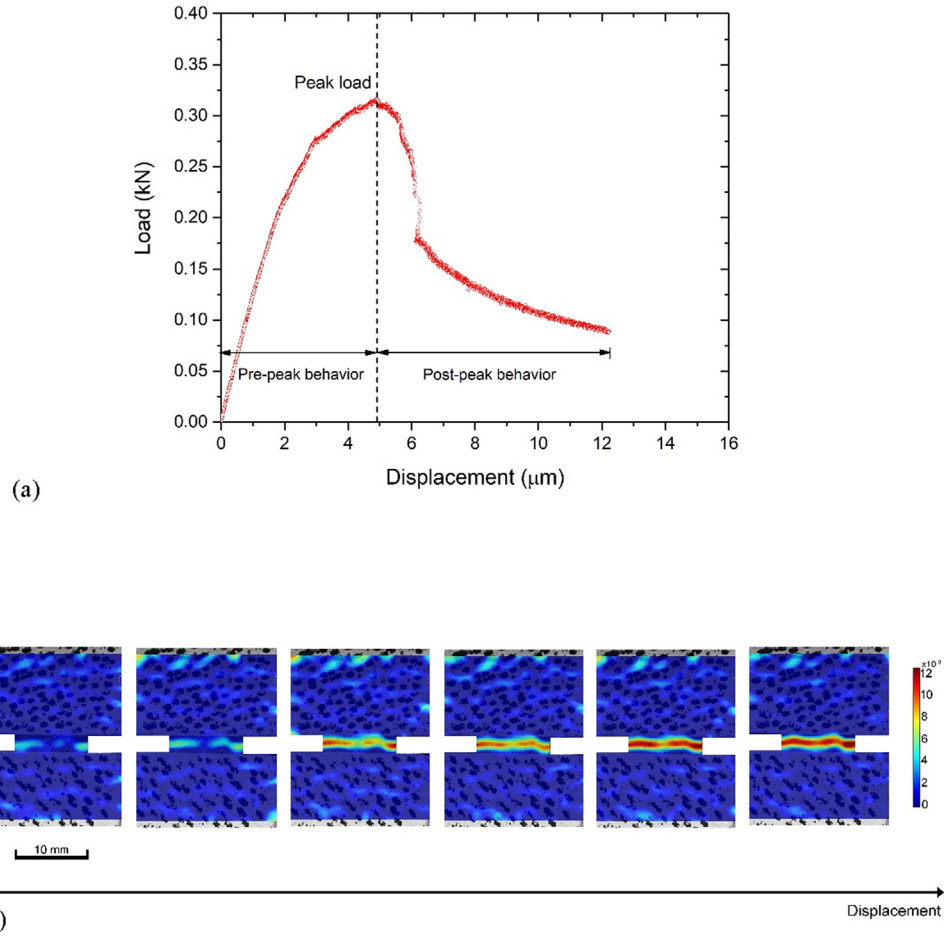

Fig. 12. An example: (a) a typical load and displacement curve of the uniaxial tensile test and (b) the corresponding DIC analysis of the specimen.

For each specimen, 40 longitudinal cross-sections of greyscale value (GSV) images were extracted from the reconstructed 3D volume (see Fig. 6). For segmenting the air voids, the so-called tangent-slope method [50,51] (illustrated in Fig. 7) was applied to the cumulative histogram. An example of the segmented binary image is shown in Fig. 8. It should be noted that only pores larger than the X-ray CT resolution (50 μm) can be detected in this manner. The air void content and distribution of each segmented binary image could be determined through a MATLAB-code (see Fig. 8).

3. Modeling

Due to its simplicity and efficiency, the discrete lattice model has been widely used to simulate the mechanical properties of cementitious materials, at both microscale [44,51,52] and mesoscale [53,54]. The model uses a lattice of Timoshenko beam elements to discretize the material domain. All the elements have a linear elastic behavior (note that it is possible to assign a ductile constitutive law of the local element, as shown in [40]). Cracks are generated by removing the element in which stress exceeds its strength under a specific boundary condition. In the case of heterogeneous materials, the heterogeneity is easily introduced by overlapping the digitalized material structure on the lattice and assigning different local mechanical properties to the elements according to their positions.

In the current study, the segmented 2D material structure with a height of 24 mm and a length of 20 mm (480 × 400 pixel^2) was used to build a series of 2D models. Two notches (with the size of 3 mm in height and 5 mm in length) were created in the meshes at mid-height (see Fig. 9). As shown in Fig. 10, a quadrangular grid of square cells was first defined, in which a node was then randomly positioned within a concentric sub-cell. According to a previous study [55], a ratio of 0.5 between the length of the cell and sub-cell can introduce the geometry disorder in the digital cementitious material while avoiding significant variations in the length of elements. Therefore, this ratio was consistently adopted herein. Delaunay triangulation was performed on the set of the defined notes, on the basis of which nodes in adjacent Voronoi cells are connected by the beam elements. This mesh configuration results in a Poisson's ratio of 0.18 [56], which is realistic for cementitious materials [57].

At the investigated length scale, the 2D material structure was considered as a two-phase structure, i.e., solid and pore phases. As shown in Fig. 10, the element that has one/two nodes located in the pore or notch area was then removed from the system as the initial flaw embedded in the material. As a simplification, all the elements located in the solid phase are assumed having the same mechanical properties, i.e., elastic modulus and tensile strength (Note that no local compressive failure is needed to simulate fracture performance of such material under uniaxial tension [55]). Those two mechanical properties were assumed to correspond with those of the mold-cast samples to investigate the influence of the pore structure on the global mechanical performance of the specimens and further explain the experimental observations. The computational uniaxial tension test was achieved by applying

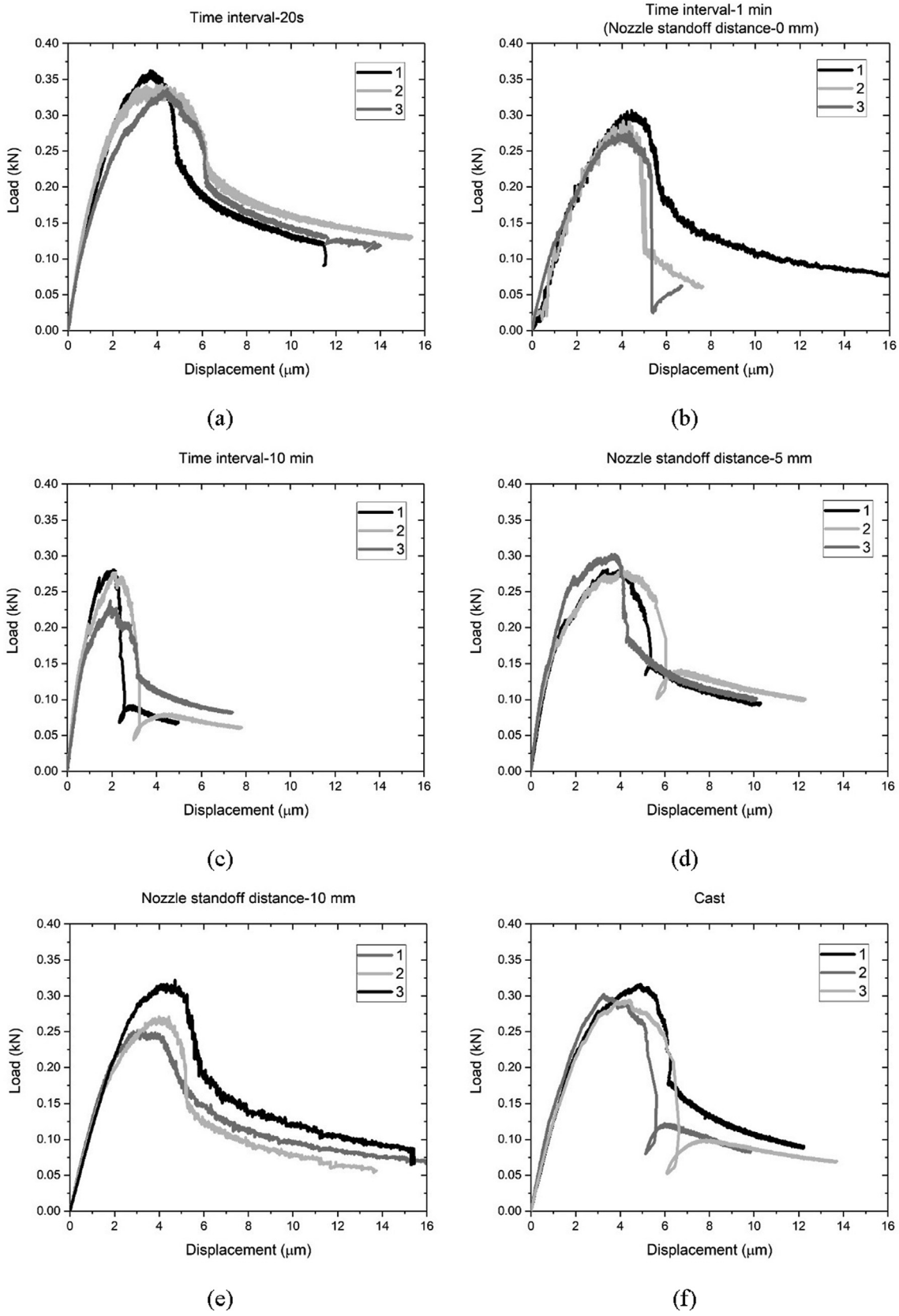

Fig. 13. Load vs. displacement curves of uniaxial tensile tests at the material age of 7 days: (a) Time interval-20 s; (b) Time interval-1 min (also known as nozzle standoff distance-0 mm); (c) Time interval-10 min; (d) Nozzle standoff distance-5 mm; (e) Nozzle standoff distance-10 mm; (f) Cast.

uniform displacement of the nodes on one side and blocking the degrees of freedom of the nodes in the opposite side (see Fig. 11). It is worth to mention that in order to simulate the boundary constraints between the steel plates and specimen in the experiments, lateral deformation and rotation of the nodes at the boundaries were fixed. In order to consider the variation of the 2D material structure, for each case, 3 simulations were carried out on the basis of 2D slices extracted from different locations (see Fig. 6).

4. Results and discussion

4.1. Uniaxial tensile strength

All load and displacement curves of the uniaxial tension tests are given in Fig. 13. The displacement of each test was the average value of two LVDTs. All specimens showed brittle behavior in tension. A similar pattern of the load and displacement curve was observed. As shown in Fig. 12 (a), the load initially increased quasi-linearly with increasing vertical displacement until reaching the peak load. Except for the specimens with a 10 min time gap (in Fig. 13 (c)), the peak load corresponded to a displacement of 4–5 μm (in Fig. 13 (a), (b), (d), (e), (f)). After the peak load, a load decrease was observed as deformations grow. In Fig. 12 (b), the color close to red in the DIC image represented the region suffering high deformation and containing cracks [63]. It could be found that two cracks nucleated from both notch tips, and then continued propagating. Finally, both cracks formed at the interface. The peak load in this test could be regarded as the ultimate interlayer bond force of the specimen. The peak force of each curve from Fig. 13 was collected and divided by the cross-section area (10×10 mm^2) to compute the uniaxial tensile bond strength. The calculated results were presented in Fig. 14.

4.1.1. Time interval

Fig. 14 (a) shows the average uniaxial tensile strength of the printed specimens (different time intervals between two adjacent layers). The uniaxial tensile strength decreased with increasing time gap, which agreed well with the earlier studies [4,9,32]. In comparison with the mold-cast specimen, a reduction in uniaxial tensile strength of about 4%, and 13% were observed in the specimens with a 1 min and 10 min time intervals, respectively. However, the specimens with a 20 s of time gap exhibited 14% increase in uniaxial tensile strength.

4.1.2. Nozzle standoff distance

The effect of nozzle standoff distance on the tensile bond strength of two layers was not critical in this study. Only a slight decrease could be found with increasing the nozzle height in Fig. 14 (b). The results of the specimens with a 10 mm nozzle standoff distance were more scattered than others, which was in accordance with the observation from Wolfs et al. [4]. However, due to the differences in nozzle type and mixture, the obtained results in this study could not be comparable with the finding of Panda et al. [9].

4.2. Air void content and distribution

The air void content and distribution of each GSV image is presented in Fig. 15. The term porosity could be referred to as air void content in this context. It could be found that the porosity in the middle zone of the printed specimens was higher than in other areas, which was due to the presence of the interface. In contrast to the printed sample, the air void distribution of the cast sample was more homogeneous. For the printed sample, the interlayer

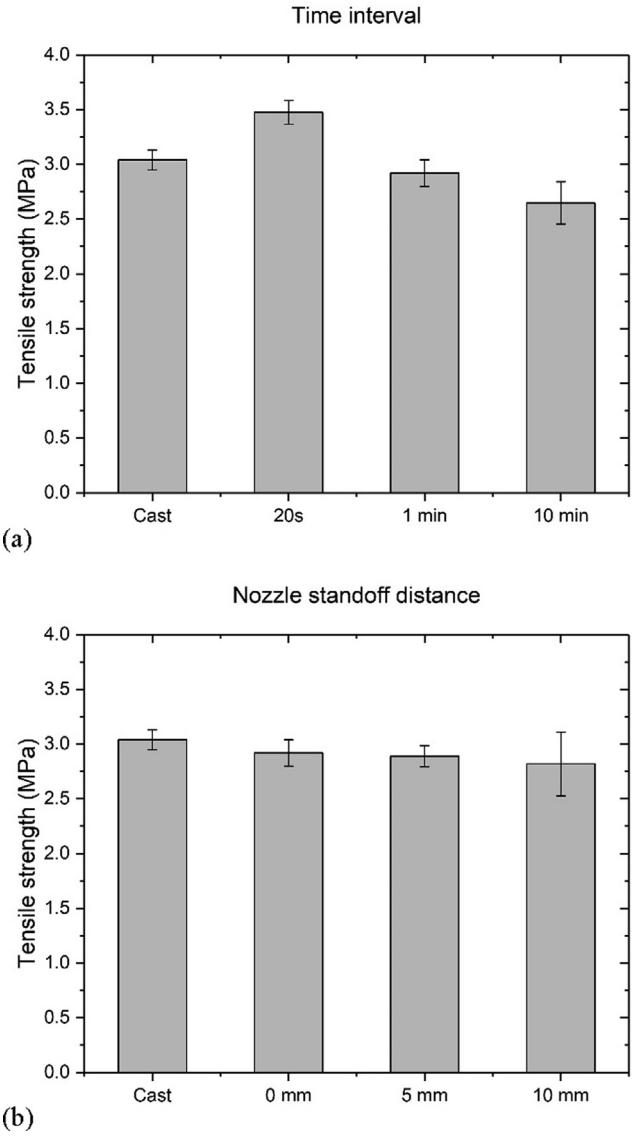

Fig. 14. Uniaxial tensile strength results at the material age of 7 days: (a) Different time intervals; (b) Different nozzle standoff distances.

zone could be located mid-height of the sample, with the height ranging from 10.5 mm to 13.5 mm. It was also the region to make notches. In general, for a quasi-brittle material, the mechanical properties are inversely proportional to the porosity [37]. Since the crack is localized in the interlayer zone, the strength of the specimens is mainly determined by the porosity within this area. The total porosity in the interlayer zone is therefore investigated and plotted in Fig. 16 (a). However, as shown in Fig. 16 (a), the results of the total porosity in the interlayer zone were very close between different specimens, except for the 10 min and cast cases. Both of them displayed higher porosity than others. As reported by Lee et al.[58], the total fraction of pores in the interlayer may not directly affect the bond strength of printed samples. Compared with the total porosity in the interlayer zone, the maximum value of local porosity seems to be a more critical factor to dominate the bond strength (see Fig. 16(b)).

4.2.1. Time interval

In Fig. 16 (b), the maximum value of local porosity in the interlayer zone increased with the increase of time interval, which is in good agreement with the interlayer bond strength in Section 4.1.

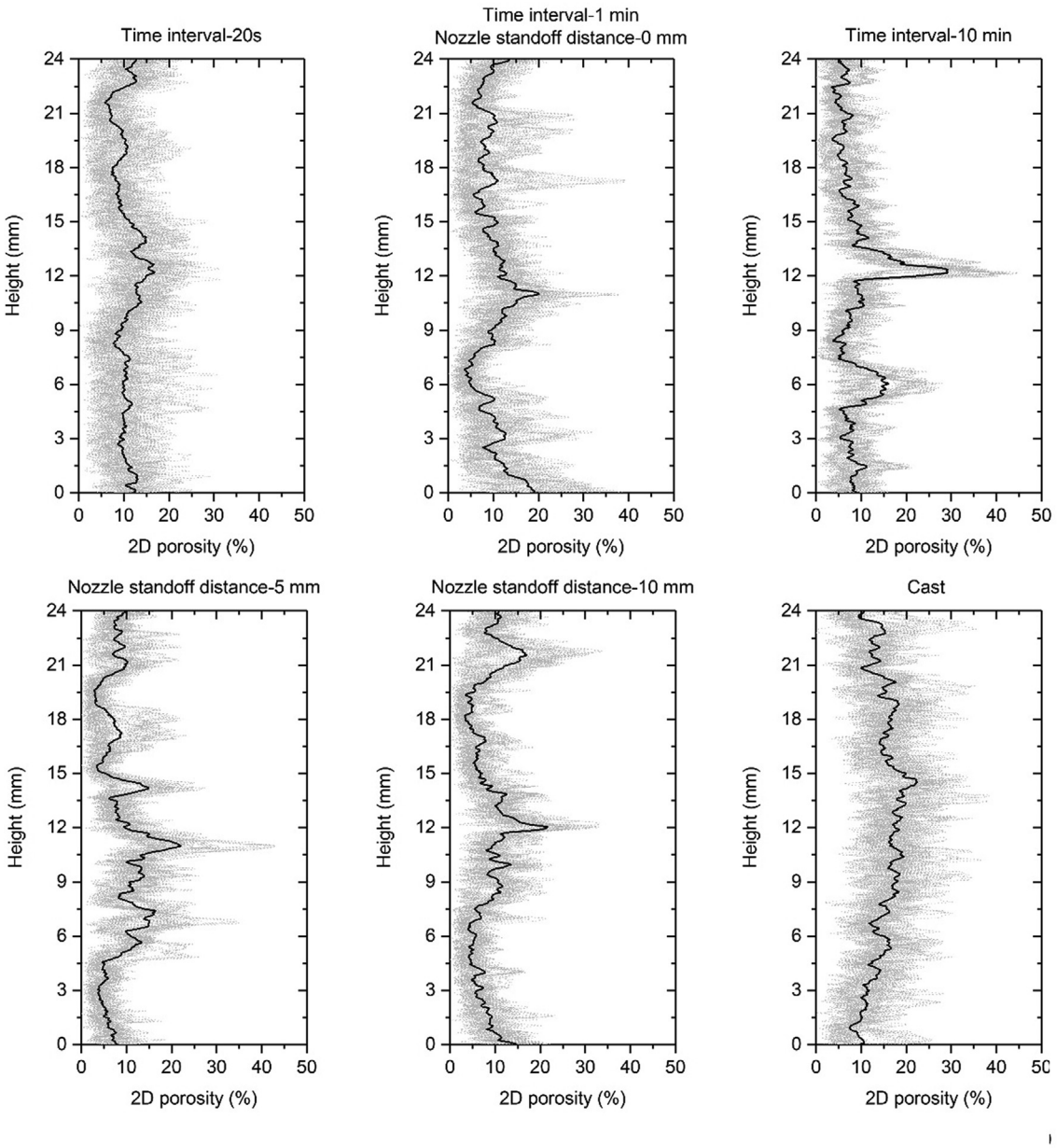

Fig. 15. Air void content and distribution (local porosity) of different samples made with various printing parameters. The grey line represents the individual computed result. The black line indicates the average relation.

The specimen with a 20 s of time interval shows the minimum value of average local porosity at the interface (Fig. 16 (b)) among all specimens, which seems to be the main reason for its highest bond strength in Fig. 14. Extending the time interval between two layers may lead to a high concentration of macropores distributed along the interface, which is a possible reason for the higher maximum value of local porosity in the interlayer zone of sample 10 min. As shown in Fig. 17, the extruded layer exhibited a rough top surface. For a short-time gap (20 s and 1 min in this study), the stress from the upper layer could result in a slight deformation of the bottom layer. Since the substrate has a relatively lower surface tension, the load induced by the weight of the top layer might rearrange the orientation of the top surface of the substrate (bottom layer), and it might increase the interacted bond area between two layers [31]. However, after 10 min, the deformation of the substrate (after depositing the top layer) may be decreased due to the growth of material stiffness that is attributed to the cement particle nucleation and surface drying process. The surface tension of the bottom layer was also increased. It results in less amount of interacted bond areas between the old and new layers. Many unfilled areas were kept forming the 'wide' macropores between two layers. This is also evident in Fig. 18. In comparison with other samples, sample 10 min showed massive macropores that have large pore widths (>2 mm). Most of those macropores distributed at the sample height of 12–13 mm. Consequently, for sample 10 min, the maximum value of local porosity was also found in this height range (see Fig. 15). Therefore, extending the time interval could increase the number of 'wide' macropores at the interface area, which increased the value of local porosity.

4.2.2. Nozzle standoff distance

The samples made with different nozzle standoff distances showed a close result of the maximum value of local porosity in the interlayer zone in Fig. 16 (b). As mentioned earlier, the dropped layer process, because of the increased nozzle height, could increase the possibility of inaccurate layer deposition, which may reduce the contact area between two adjacent layers. The variable contact pressures and surface areas between two layers induced by the inaccurate layer deposition could result in the high scatter of the test results [4] (see Fig. 3 (a)). Therefore, it is essential to keep the nozzle standoff distance within a valid range during the printing process. A real-time height measurement device and a feedback system that were reported by Wolfs et al. [59] could be employed for an inline control of the nozzle standoff distance in practice.

4.3. Modeling results

4.3.1. Calibration

Through a trial-and-error process, the input elastic modulus and tensile strength of the lattice element have been determined as 25 GPa and 9 MPa, respectively. As shown in Fig. 19, with the aforementioned parameters, the modeling results of cast samples show reasonable agreement with the experimental results in terms of the pre-peak part, especially the tensile strength. The crack is localized in the middle area of the sample. However, a brittle post-peak behavior is observed in the simulation. This is mainly attributed to the fact that the constitutive relation of the local elements is assumed as elastic-brittle. As pointed by Zhang et al. [60], the strain-softening behavior at the microscale must be considered in the mesoscale model for quantitative prediction of fracture

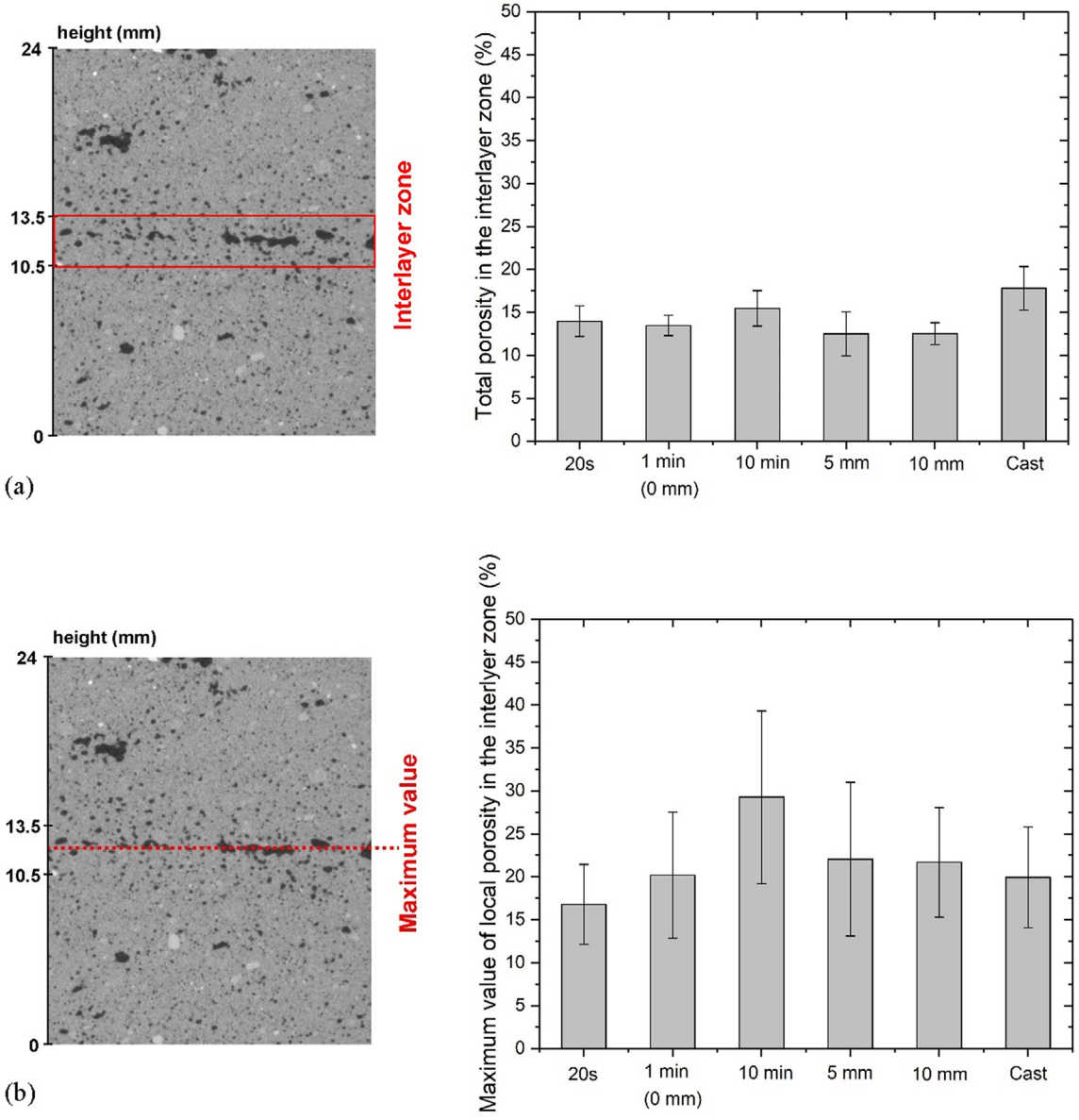

Fig. 16. (a) Total porosity in the interlayer zone; (b) The maximum value of local porosity in the interlayer zone. Interlayer zone: 10.5–13.5 mm in the height of the sample.

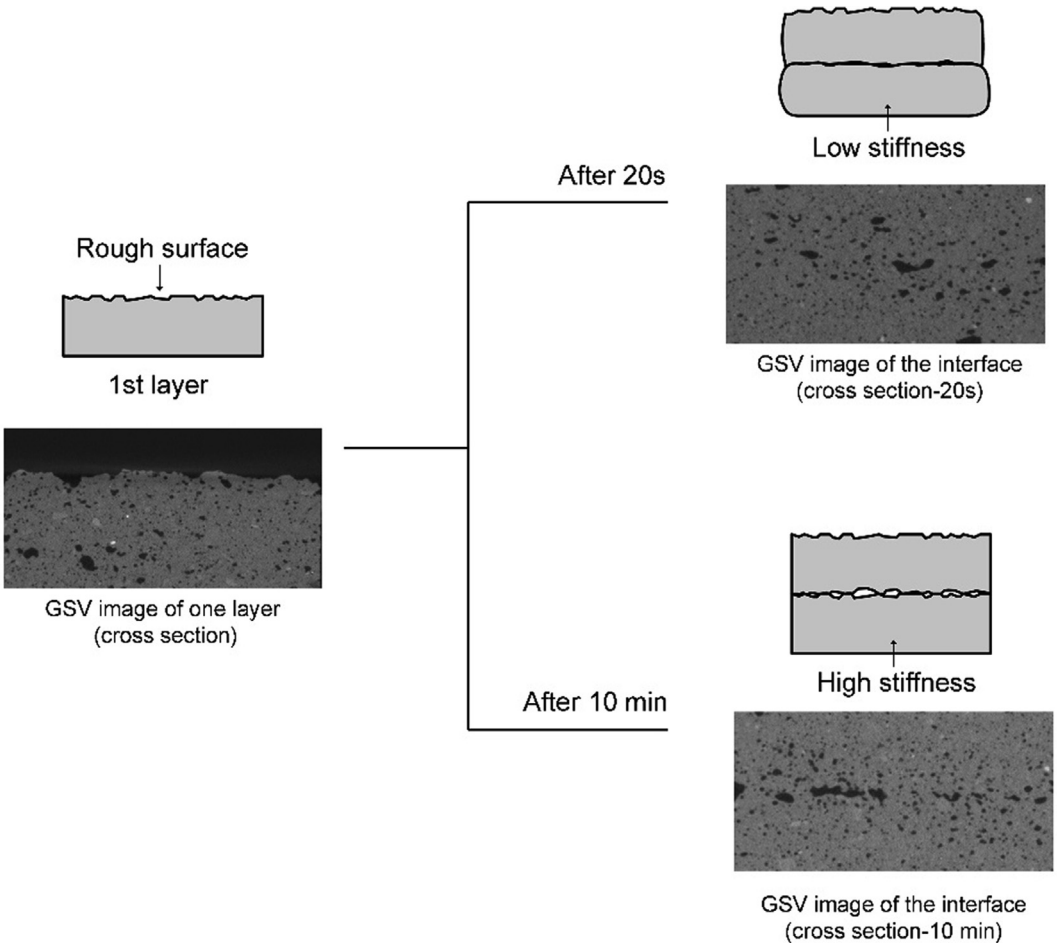

Fig. 17. Illustration of the influences of extending the time interval on air void formation at the interface.

behavior of cementitious composites. Additionally, as a 2D model was used in the current study, the crack cannot propagate out-of-plane. This also contributes to the brittle post-peak behavior. Possible solutions would be deriving the local elastoplastic constitutive relations from experiments or simulations at a lower scale (i.e., microscale) as performed in [40,41,51,52,60–62]. Nevertheless, the purpose of this paper is to show the potential of the mesoscale model and not to have an 'exact' match.

4.3.2. Modeling results

The mechanical properties of the material made from different parameters were investigated by the 2D lattice fracture model. Fig. 20 shows the simulated load–displacement curves by keeping the input but varying the 2D material structure (the segmented binary image). A variation appeared between different 2D material structures due to the heterogeneous nature of the cementitious material.

Fig. 21 (also see Fig. A.1, Appendix A) shows the fracture pattern of the simulated specimens. All the cracks are localized in the middle part of the sample, where the notches are presented. It is in accordance with the experimental observation (see Fig. 12 (b)). Besides, it can be observed that there is a tendency for cracks to propagate along the air voids, and this tendency becomes more evident in the simulated specimen with 10 min time interval. Thus, it confirmed that the local porosity in this area played a dominant role in the interlayer bond strength. Fig. 22 shows a comparison between the predicted tensile strength and experimental results. In general, the predicted results correspond well with the experiments. The only exception is specimen 10 mm due to the heterogeneous nature of the cementitious material. The predicted result is higher than the experimental result but still the error is less than 15%. Therefore, the 2D model in this study can give reasonable predictions and catch the trend of the strength variation along with the material structure.

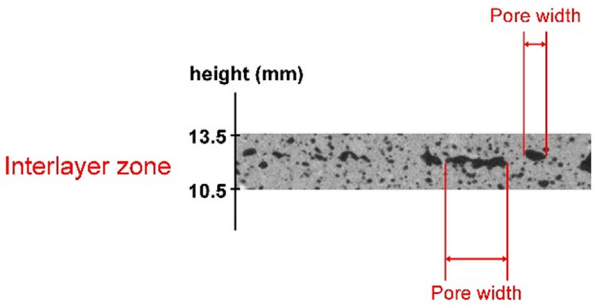

(a)

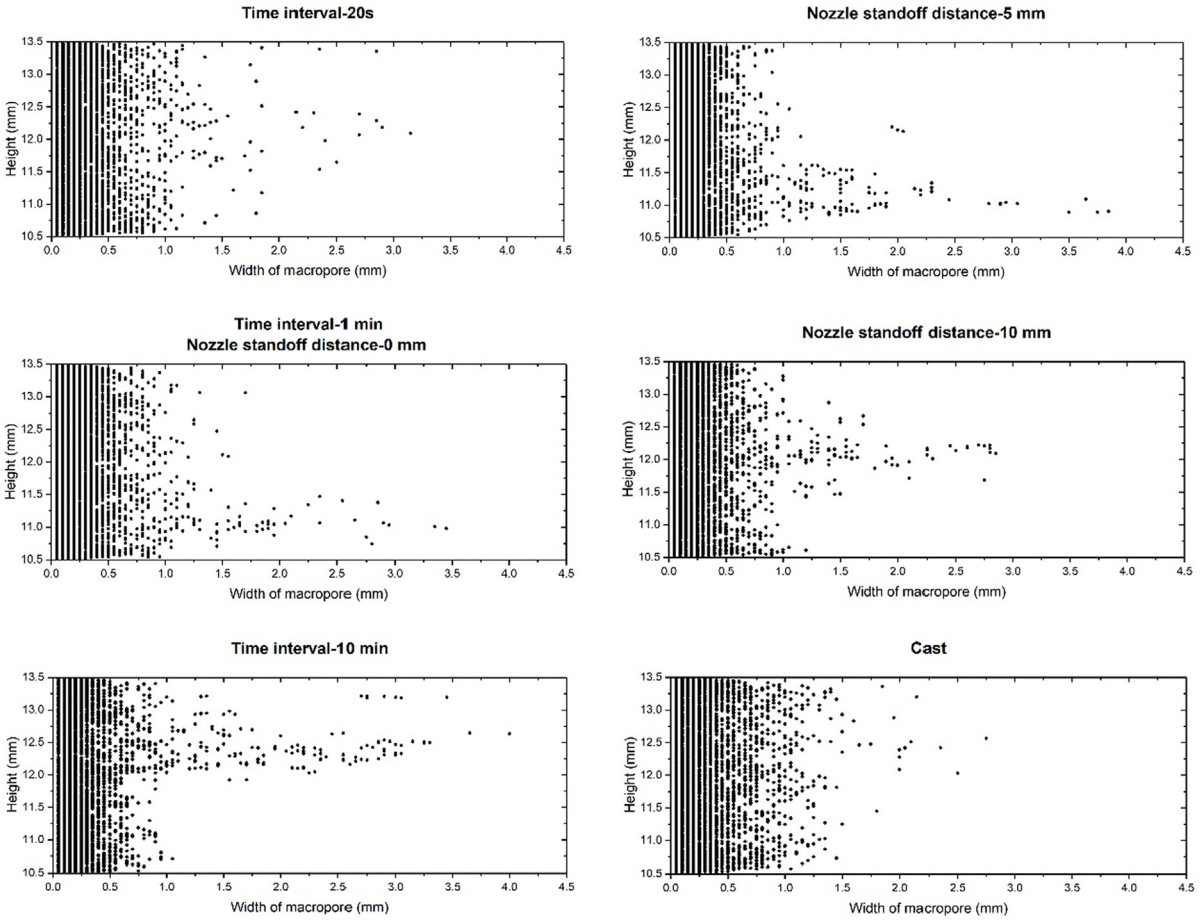

(b)

Fig. 18. (a) Illustration of pore width determination; (b) Pore width distribution of different samples (results of 40 cross-sections for each sample were plotted) in the interlayer zone (10.5–13.5 mm in height).

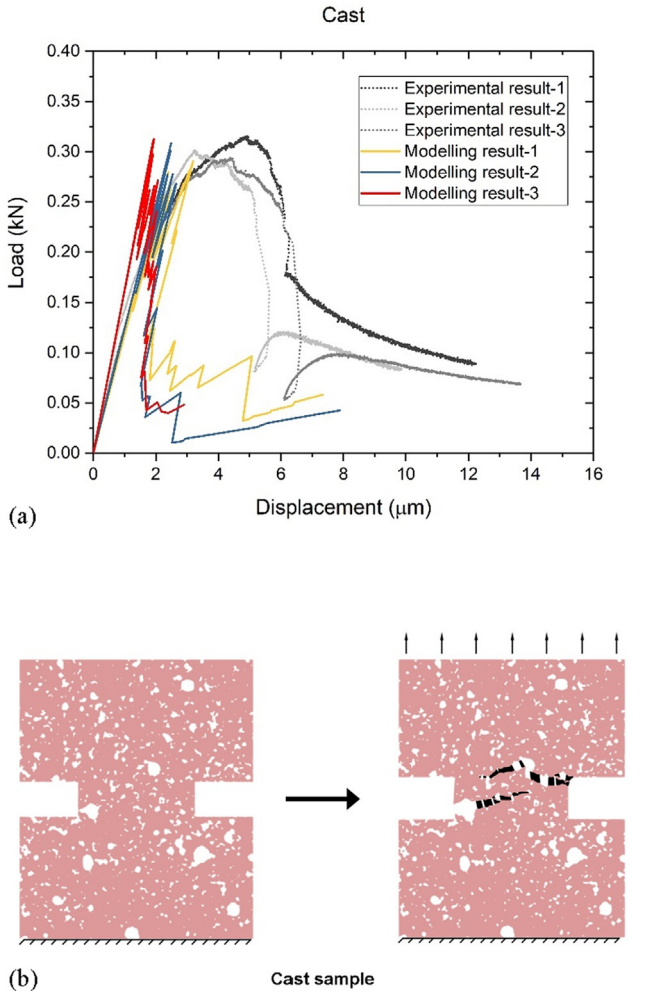

Fig. 19. (a) The simulated load–displacement curves of the cast specimens; (b) The simulated crack pattern (left: initial specimen; right: fractured specimen). Pink area-cementitious material; White area-air void. Black area-crack opening. (For interpretation of the references to color in this figure legend, the reader is referred to the web version of this article.)

5. Conclusion

An experimental and numerical study has been presented to map the effects of different printing parameters, including the time intervals and nozzle standoff distances, on the interlayer bond strength of 3D printed limestone and cementitious materials for a single batch material. Through performing the uniaxial tensile test under a non-rotational boundary condition, the load vs. displacement curve (including the softening branch) and the bond strength of printed specimens were obtained. Besides, the air void content and distribution of the printed specimens were conducted via X-ray computed tomography and image analysis. Furthermore, the acquired GSV images were employed as the input of a 2D lattice fracture model for simulating the process of uniaxial tensile test. The following conclusions could be drawn in this paper:

- The specimen with a 20 s of time interval showed the highest interlayer bond strength compared to that of other specimens, which may be attributed to its lowest local porosity at the interface. As the increment of the time interval (from 1 min to 10 min), the interlayer bond strength of printed specimens was reduced at most 13% in comparison with the cast specimens. The reduction in bond strength with prolonging the time interval was due to the increase of local porosity, which was attributed to the increased number of 'wide' macropores (pore width > 2 mm) in the interlayer zone.
- By increasing the nozzle standoff distance, limited effects on bond strength in the interlayer zone have been observed. The possibility of inaccurate layer deposition was increased by increasing the nozzle height, which increased the scatter of uniaxial tensile test results.
- The predicted results of bond strength from the 2D lattice fracture model corresponded well with the experimental results of the uniaxial tensile test. In the model, the local strength of the elements is not changed when the time interval between the layers increases. Since the predicted strength is similar between experiment and model, it can be concluded that the effect of short time intervals (20 s–10 min) has no (or minimal) influence on the bonding of the material. The strength seems to be only influenced by the local porosity. If the time interval would increase further, the bonding between the materials is probably also affected.
- Due to the limitation of the 2D lattice fracture model, it is worthwhile to employ a 3D lattice fracture model to obtain more insights in the fracture mechanics of 3D printed cementitious materials in further study.

CRediT authorship contribution statement

Yu Chen: Conceptualization, Data curation, Formal analysis, Funding acquisition, Investigation, Methodology, Validation, Visualization, Writing - original draft, Writing - review & editing. **Koen Jansen:** Investigation, Validation, Writing - review & editing. **Hongzhi Zhang:** Conceptualization, Data curation, Formal analysis, Software, Methodology, Validation, Writing - original draft, Writing - review & editing. **Claudia Romero Rodriguez:** Investigation, Validation, Writing - review & editing. **Yidong Gan:** Investigation, Validation, Writing - review & editing. **Oğuzhan Çopuroğlu:** Conceptualization, Funding acquisition, Project administration, Resources, Supervision, Writing - review & editing. **Erik Schlangen:** Conceptualization, Funding acquisition, Project administration, Resources, Supervision, Writing - review & editing.

Declaration of Competing Interest

The authors declare that they have no known competing financial interests or personal relationships that could have appeared to influence the work reported in this paper.

Acknowledgments

Yu Chen and Yidong Gan would like to acknowledge the funding supported by China Scholarship Council under grant No. 201807720005 and No. 201706130140, respectively. Hongzhi Zhang acknowledges the financial support from Taishan Scholars Program of Shandong Province under grant number tsqn201909032. Claudia Romero Rodriguez acknowledges the financial support from the Construction Technology Research Program funded by the Ministry of Land, Infrastructure, and Transport of the Korean Government under the grant 17SCIP-B103706-03. The authors appreciate Mr. Stefan Chaves Figueiredo, Mr. Arjan Thijssen, and Mr. Maiko van Leeuwen for their supports in conducting the tests. Burgess Pigment Company is thanked for the supply of the Optipozz®Burgess metakaolin.

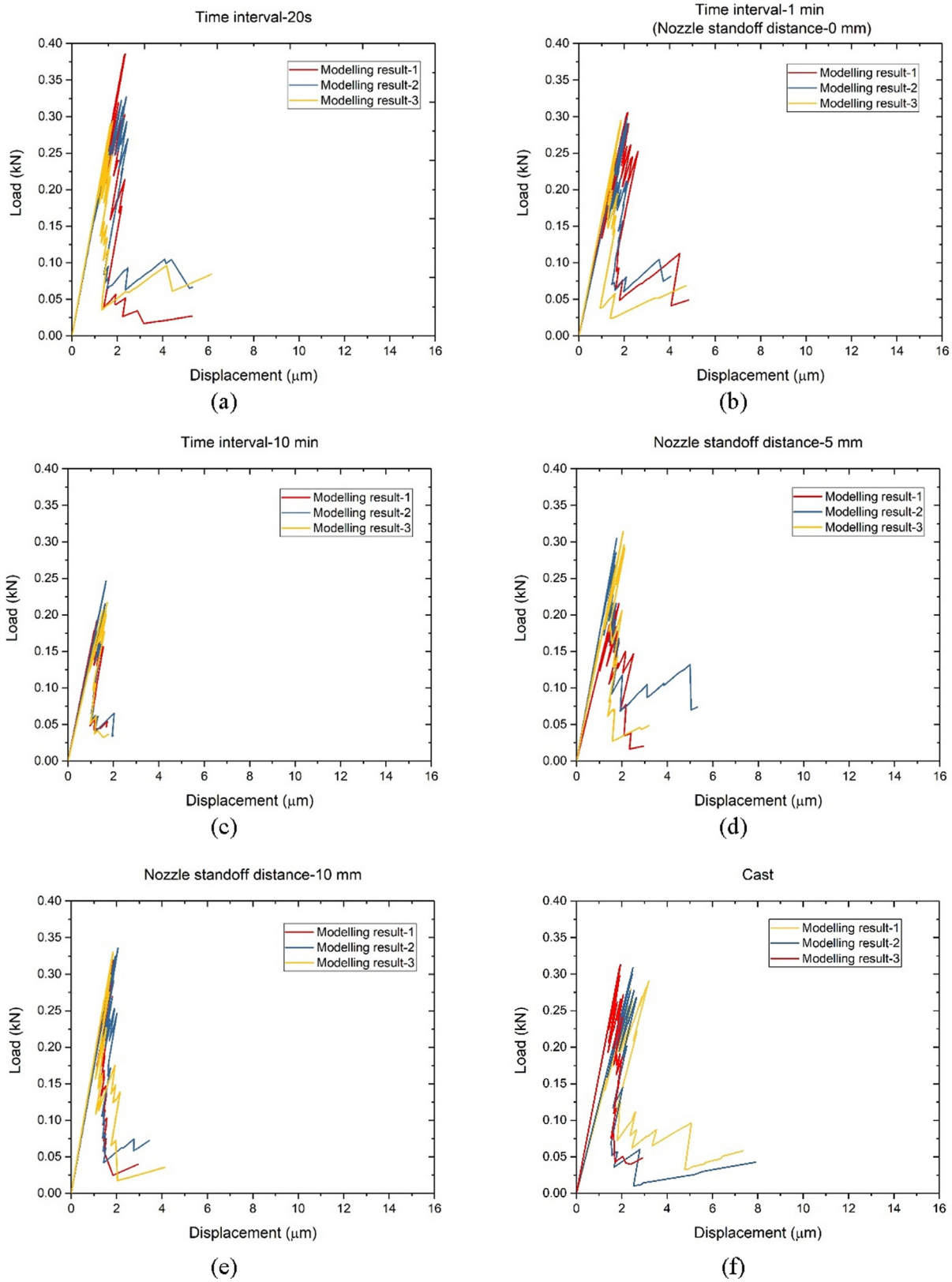

Fig. 20. Simulated load vs. displacement curves of uniaxial tension tests: (a) Time interval-20 s; (b) Time interval-1 min (and also known as nozzle standoff distance-0 mm); (c) Time interval-10 min; (d) Nozzle standoff distance-5 mm; (e) Nozzle standoff distance-10 mm; (f) Cast.

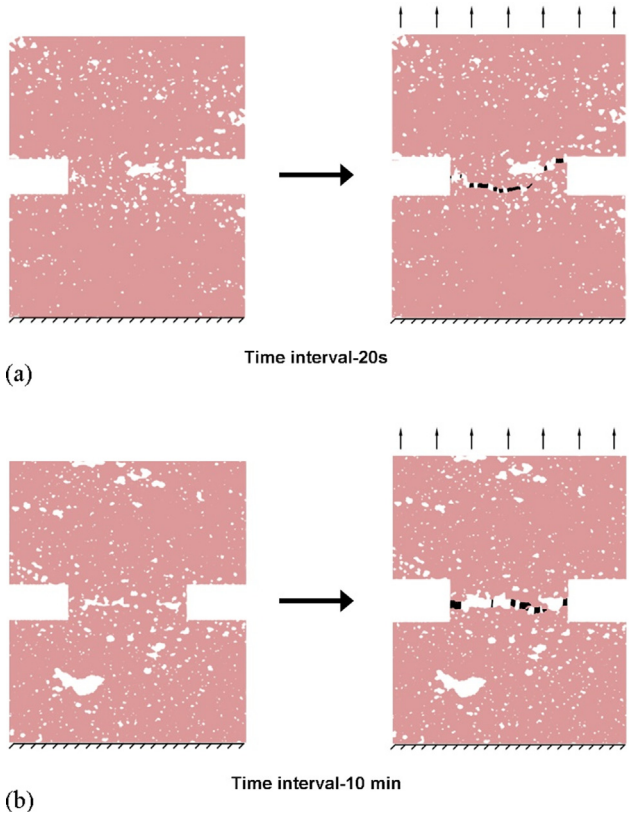

Fig. 21. The simulated fracture patterns for different printed specimens (left: initial specimen; right: fractured specimen): (a) Time interval-20 s; (b) Time interval-10 min. Pink area-cementitious material; White area-air void. Black area-crack opening. (For interpretation of the references to color in this figure legend, the reader is referred to the web version of this article.)

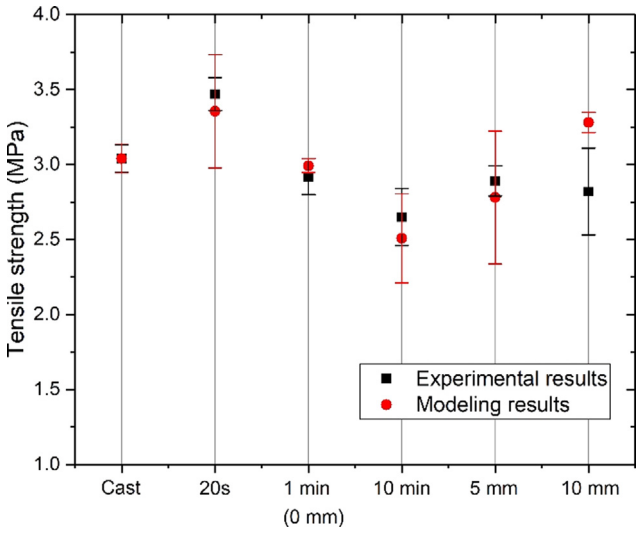

Fig. 22. Comparison between the modeling and experimental results.

Appendix A

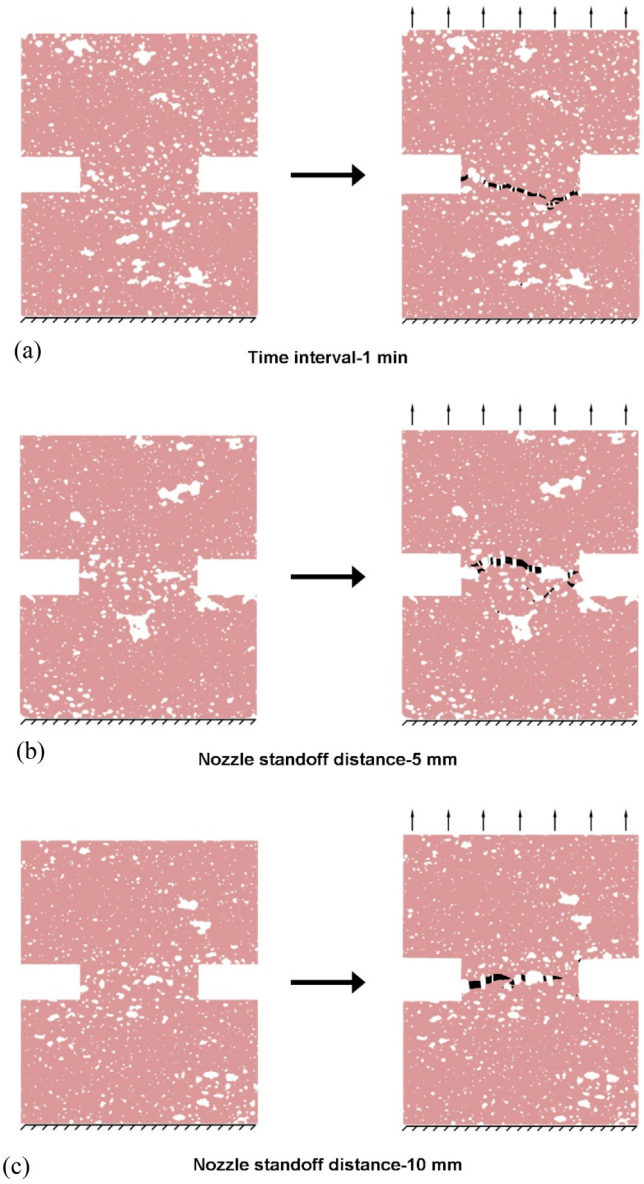

Fig. A1. The simulated fracture patterns for different printed specimens (left: initial specimen; right: fractured specimen).: (a) Time interval-1 min; (b) Nozzle standoff distance-5 mm; (c) Nozzle standoff distance-10 mm. Pink area-cementitious material; White area-air void. Black area-crack opening.

References

[1] R.A. Buswell, W.R. Leal de Silva, S.Z. Jones, J. Dirrenberger, 3D printing using concrete extrusion: a roadmap for research, Cem. Concr. Res. 112 (2018) 37–49, https://doi.org/10.1016/j.cemconres.2018.05.006.

[2] Y. Chen, Z. Li, S. Chaves Figueiredo, O. Çopuroğlu, F. Veer, E. Schlangen, Limestone and calcined clay-based sustainable cementitious materials for 3D concrete printing: a fundamental study of extrudability and early-age strength development, Appl. Sci. 9 (2019) 1809, https://doi.org/10.3390/app9091809.

[3] Y. Chen, F. Veer, O. Çopuroğlu, A critical review of 3D concrete printing as a low CO 2 concrete approach, Heron. 62 (2017) 167–194.

[4] R.J.M. Wolfs, F.P. Bos, T.A.M. Salet, Hardened properties of 3D printed concrete: the influence of process parameters on interlayer adhesion, Cem. Concr. Res. 119 (2019) 132–140, https://doi.org/10.1016/j.cemconres.2019.02.017.

[5] F. Bos, R. Wolfs, Z. Ahmed, T. Salet, Additive manufacturing of concrete in construction: potentials and challenges of 3D concrete printing, Virtual Phys. Prototyp. 11 (2016) 209–225, https://doi.org/10.1080/17452759.2016.1209867.

[6] L. Reiter, T. Wangler, N. Roussel, R.J. Flatt, The role of early age structural build-up in digital fabrication with concrete, Cem. Concr. Res. 112 (2018) 86–95, https://doi.org/10.1016/j.cemconres.2018.05.011.

[7] S.C. Paul, Y.W.D. Tay, B. Panda, M.J. Tan, Fresh and hardened properties of 3D printable cementitious materials for building and construction, Arch. Civ. Mech. Eng. 18 (2018) 311–319, https://doi.org/10.1016/j.acme.2017.02.008.

[8] Y. Chen, S. Chaves Figueiredo, Ç. Yalçinkaya, O. Çopuroğlu, F. Veer, E. Schlangen, The effect of viscosity-modifying admixture on the extrudability of limestone and calcined clay-based cementitious material for extrusion-based 3D concrete printing, Materials (Basel) 12 (2019) 1374, https://doi.org/10.3390/ma12091374.

[9] B. Panda, S.C. Paul, N.A.N. Mohamed, Y.W.D. Tay, M.J. Tan, Measurement of tensile bond strength of 3D printed geopolymer mortar, Meas. J. Int. Meas. Confed. 113 (2018) 108–116, https://doi.org/10.1016/j.measurement.2017.08.051.

[10] T.T. Le, S.A. Austin, S. Lim, R.A. Buswell, A.G.F. Gibb, T. Thorpe, Mix design and fresh properties for high-performance printing concrete, Mater. Struct. 45 (2012) 1221–1232, https://doi.org/10.1617/s11527-012-9828-z.

[11] C. Zhang, Z. Hou, C. Chen, Y. Zhang, V. Mechtcherine, Z. Sun, Design of 3D printable concrete based on the relationship between flowability of cement paste and optimum aggregate content, Cem. Concr. Compos. 104 (2019), https://doi.org/10.1016/j.cemconcomp.2019.103406 103406.

[12] B. Panda, C. Unluer, M.J. Tan, Investigation of the rheology and strength of geopolymer mixtures for extrusion-based 3D printing, Cem. Concr. Compos. 94 (2018) 307–314, https://doi.org/10.1016/j.cemconcomp.2018.10.002.

[13] Y. Chen, F. Veer, O. Copuroglu, E. Schlangen, Feasibility of Using Low CO2 Concrete Alternatives in Extrusion-Based 3D Concrete Printing, in: T. Wangler, R. Flatt (Eds.), First RILEM Int. Conf. Concr. Digit. Fabr. – Digit. Concr, Springer, Cham, 2019, pp. 269–276, https://doi.org/10.1007/978-3-319-99519-9_25.

[14] K. Scrivener, F. Martirena, S. Bishnoi, S. Maity, Calcined clay limestone cements (LC3), Cem. Concr. Res. 114 (2018) 49–56, https://doi.org/10.1016/j.cemconres.2017.08.017.

[15] F. Martirena, K. Scrivener, Low carbon cement LC3 in Cuba: Ways to achieve a sustainable growth of cement production in emerging economies, in: Proc. 2nd Int. Conf. Calcined Clays Sustain. Concr., 2018, pp. 318–321. doi:10.1007/978-94-024-1207-9_51.

[16] S. Bishnoi, S. Maity, Limestone calcined clay cement: The experience in India this far, in: Proc. 2nd Int. Conf. Calcined Clays Sustain. Concr., 2018, pp. 64–68. doi:10.1007/978-94-024-1207-9_11.

[17] M. Antoni, J. Rossen, F. Martirena, K. Scrivener, Cement substitution by a combination of metakaolin and limestone, Cem. Concr. Res. 42 (2012) 1579–1589, https://doi.org/10.1016/j.cemconres.2012.09.006.

[18] F. Avet, R. Snellings, A. Alujas Diaz, M. Ben Haha, K. Scrivener, Development of a new rapid, relevant and reliable (R3) test method to evaluate the pozzolanic reactivity of calcined kaolinitic clays, Cem. Concr. Res. 85 (2016) 1–11, https://doi.org/10.1016/j.cemconres.2016.02.015.

[19] F. Avet, K. Scrivener, Investigation of the calcined kaolinite content on the hydration of Limestone Calcined Clay Cement (LC3), Cem. Concr. Res. 107 (2018) 124–135, https://doi.org/10.1016/j.cemconres.2018.02.016.

[20] F. Avet, E. Boehm-Courjault, K. Scrivener, Investigation of C-A-S-H composition, morphology and density in Limestone Calcined Clay Cement (LC3), Cem. Concr. Res. 115 (2019) 70–79, https://doi.org/10.1016/j.cemconres.2018.10.011.

[21] Chen Y, Yalçınkaya Ç, Çopuroğlu O, et al. The Effect Of Viscosity Modifier Agent On The Early Age Strength Of The Limestone And Calcined Clay-Based Sustainable And 3D Printable Cementitious Material[J]. Proc. 10th Int. Concr. Congr., Bursa Akademik Odalar Birliği, 2019: 242–250.

[22] Y. Chen, S. Chaves Figueiredo, Z. Li, Z. Chang, K. Jansen, O. Çopuroğlu, E. Schlangen, Improving printability of limestone-calcined clay-based cementitious materials by using viscosity-modifying admixture, Cem. Concr. Res. 132 (2020), https://doi.org/10.1016/j.cemconres.2020.106040 106040.

[23] Y. Chen, C. Romero Rodriguez, L. Zhenmin, C. Boyu, O. Copuroglu, E. Schlangen, Effect of different grade levels of calcined clays on fresh and hardened properties of ternary-blended cementitious materials for 3D printing, Cem, Concr. Compos. (2020) 103708, https://doi.org/10.1016/j.cemconcomp.2020.103708. In press.

[24] A. Perrot, D. Rangeard, A. Pierre, Structural built-up of cement-based materials used for 3D-printing extrusion techniques, Mater. Struct. 49 (2016) 1213–1220, https://doi.org/10.1617/s11527-015-0571-0.

[25] N. Roussel, F. Cussigh, Distinct-layer casting of SCC: The mechanical consequences of thixotropy, Cem. Concr. Res. 38 (2008) 624–632, https://doi.org/10.1016/j.cemconres.2007.09.023.

[26] N. Roussel, Rheological requirements for printable concretes, Cem. Concr. Res. 112 (2018) 76–85, https://doi.org/10.1016/j.cemconres.2018.04.005.

[27] B. Zareiyan, B. Khoshnevis, Effects of interlocking on interlayer adhesion and strength of structures in 3D printing of concrete, Autom. Constr. (2017), https://doi.org/10.1016/j.autcon.2017.08.019.

[28] T. Wangler, E. Lloret, L. Reiter, N. Hack, F. Gramazio, M. Kohler, M. Bernhard, B. Dillenburger, J. Buchli, N. Roussel, R. Flatt, Digital concrete: opportunities and challenges, RILEM Tech. Lett. 1 (2016) 67, https://doi.org/10.21809/rilemtechlett.2016.16.

[29] N. Roussel, G. Ovarlez, S. Garrault, C. Brumaud, The origins of thixotropy of fresh cement pastes, Cem. Concr. Res. 42 (2012) 148–157, https://doi.org/10.1016/j.cemconres.2011.09.004.

[30] B. Panda, N.A.N. Mohamed, S.C. Paul, G.V.P.B. Singh, M.J. Tan, B. Šavija, The effect of material fresh properties and process parameters on buildability and interlayer adhesion of 3D printed concrete, Materials (Basel). 12 (2019) 2149, https://doi.org/10.3390/ma12132149.

[31] Y.W.D. Tay, G.H.A. Ting, Y. Qian, B. Panda, L. He, M.J. Tan, Time gap effect on bond strength of 3D-printed concrete, Virtual Phys. Prototyp. 14 (2019) 104–113, https://doi.org/10.1080/17452759.2018.1500420.

[32] T.T. Le, S.A. Austin, S. Lim, R.A. Buswell, R. Law, A.G.F. Gibb, T. Thorpe, Hardened properties of high-performance printing concrete, Cem. Concr. Res. 42 (2012) 558–566, https://doi.org/10.1016/j.cemconres.2011.12.003.

[33] E. Keita, H. Bessaies-Bey, W. Zuo, P. Belin, N. Roussel, Weak bond strength between successive layers in extrusion-based additive manufacturing: measurement and physical origin, Cem. Concr. Res. 123 (2019), https://doi.org/10.1016/j.cemconres.2019.105787 105787.

[34] V.N. Nerella, S. Hempel, V. Mechtcherine, Effects of layer-interface properties on mechanical performance of concrete elements produced by extrusion-based 3D-printing, Constr. Build. Mater. 205 (2019) 586–601, https://doi.org/10.1016/j.conbuildmat.2019.01.235.

[35] J.G. Sanjayan, B. Nematollahi, M. Xia, T. Marchment, Effect of surface moisture on inter-layer strength of 3D printed concrete, Constr. Build. Mater. 172 (2018) 468–475, https://doi.org/10.1016/j.conbuildmat.2018.03.232.

[36] J. Van Der Putten, G. De Schutter, K. Van Tittelboom, Surface modification as a technique to improve inter-layer bonding strength in 3D printed cementitious materials, RILEM Tech. Lett. 4 (2019) 33–38, https://doi.org/10.21809/rilemtechlett.2019.84.

[37] D. Liu, B. Šavija, G.E. Smith, P.E.J. Flewitt, T. Lowe, E. Schlangen, Towards understanding the influence of porosity on mechanical and fracture behaviour of quasi-brittle materials: experiments and modelling, Int. J. Fract. 205 (2017) 57–72, https://doi.org/10.1007/s10704-017-0181-7.

[38] T. Marchment, J. Sanjayan, M. Xia, Method of enhancing interlayer bond strength in construction scale 3D printing with mortar by effective bond area ampli fi cation, Mater. Des. 169 (2019), https://doi.org/10.1016/j.matdes.2019.107684 107684.

[39] E. Schlangen, Experimental and Numerical Analysis of Fracture Processes in Concrete, Delft University of Technology, 1993.

[40] H. Zhang, B. Šavija, S.C. Figueiredo, E. Schlangen, Experimentally validated multi-scale modelling scheme of deformation and fracture of cement paste, Cem. Concr. Res. 102 (2017) 175–186, https://doi.org/10.1016/j.cemconres.2017.09.011.

[41] H. Zhang, Y. Gan, Y. Xu, S. Zhang, E. Schlangen, B. Šavija, Experimentally informed fracture modelling of interfacial transition zone at micro-scale, Cem. Concr. Compos. 104 (2019), https://doi.org/10.1016/j.cemconcomp.2019.103383 103383.

[42] H. Zhang, B. Šavija, E. Schlangen, Combined experimental and numerical study on micro-cube indentation splitting test of cement paste, Eng. Fract. Mech. 199 (2018) 773–786, https://doi.org/10.1016/j.engfracmech.2018.04.018.

[43] B. Šavija, H. Zhang, E. Schlangen, Micromechanical testing and modelling of blast furnace slag cement pastes, Constr. Build. Mater. 239 (2020), https://doi.org/10.1016/j.conbuildmat.2019.117841 117841.

[44] H. Zhang, B. Šavija, E. Schlangen, Towards understanding stochastic fracture performance of cement paste at micro length scale based on numerical simulation, Constr. Build. Mater. 183 (2018) 189–201, https://doi.org/10.1016/j.conbuildmat.2018.06.167.

[45] M. Luković, B. Šavija, H. Dong, E. Schlangen, G. Ye, Micromechanical study of the interface properties in concrete repair systems, J. Adv. Concr. Technol. 12 (2014) 320–339, https://doi.org/10.3151/jact.12.320.

[46] B. Šavija, M. Luković, J. Pacheco, E. Schlangen, Cracking of the concrete cover due to reinforcement corrosion: a two-dimensional lattice model study, Constr. Build. Mater. 44 (2013) 626–638, https://doi.org/10.1016/j.conbuildmat.2013.03.063.

[47] Z. Qian, E. Schlangen, G. Ye, K. van Breugel, Modeling framework for fracture in multiscale scement-based material structures, Materials (Basel). 10 (2017), https://doi.org/10.3390/ma10060587.

[48] R. Wolfs, Experimental Characterization and Numerical Modelling of 3D Printed Concrete, Eindhoven University of Technology, 2019.

[49] J. Blaber, B. Adair, A. Antoniou, Ncorr: Open-Source 2D Digital Image Correlation Matlab Software, Exp. Mech. 55 (2015) 1105–1122, https://doi.org/10.1007/s11340-015-0009-1.

[50] K.L. Scrivener, Backscattered electron imaging of cementitious microstructures: understanding and quantification, Cem. Concr. Compos. 26 (2004) 935–945, https://doi.org/10.1016/j.cemconcomp.2004.02.029.

[51] H. Zhang, B. Šavija, S.C. Figueiredo, M. Lukovic, E. Schlangen, Microscale testing and modelling of cement paste as basis for multi-scale modelling, Materials (Basel). 9 (2016), https://doi.org/10.3390/ma9110907.
[52] H. Zhang, Y. Xu, Y. Gan, Z. Chang, E. Schlangen, B. Šavija, Combined experimental and numerical study of uniaxial compression failure of hardened cement paste at micrometre length scale, Cem. Concr. Res. 126 (2019), https://doi.org/10.1016/j.cemconres.2019.105925.
[53] B. Šavija, J. Pacheco, E. Schlangen, Lattice modeling of chloride diffusion in sound and cracked concrete, Cem. Concr. Compos. 42 (2013) 30–40, https://doi.org/10.1016/j.cemconcomp.2013.05.003.
[54] H. Zhang, B. Šavija, Y. Xu, E. Schlangen, Size effect on splitting strength of hardened cement paste: experimental and numerical study, Cem. Concr. Compos. 94 (2018) 264–276, https://doi.org/10.1016/j.cemconcomp.2018.09.018.
[55] E. Schlangen, E.J. Garboczi, Fracture simulations of concrete using lattice models: computational aspects, Eng. Fract. Mech. 57 (1997) 319–332, https://doi.org/10.1016/s0013-7944(97)00010-6.
[56] H. Zhang, B. Šavija, M. Luković, E. Schlangen, Experimentally informed micromechanical modelling of cement paste: an approach coupling X-ray computed tomography and statistical nanoindentation, Compos. Part B Eng. 157 (2019) 109–122, https://doi.org/10.1016/j.compositesb.2018.08.102.
[57] K. Mehta, P.J.M. Monteiro, Microstructure and properties of hardened concrete, in: Concr. Microstruct. Prop. Mater., 3rd ed., McGraw-Hill, New York, 2016, pp. 41–80.
[58] H. Lee, J.-H.J. Kim, J.-H. Moon, W.-W. Kim, E.-A. Seo, Correlation between pore characteristics and tensile bond strength of additive manufactured mortar using X-ray computed tomography, Constr. Build. Mater. 226 (2019) 712–720, https://doi.org/10.1016/j.conbuildmat.2019.07.161.
[59] R.J.M. Wolfs, F.P. Bos, E.C.F. van Strien, T.A.M. Salet, A real-time height measurement and feedback system for 3D concrete printing, in: D.A. Hordijk, M. Luković (Eds.), High Tech Concr. Where Technol. Eng. Meet - Proc. 2017 Fib Symp., Maastricht, 2017. doi:10.1007/978-3-319-59471-2.
[60] H. Zhang, Y. Xu, Y. Gan, E. Schlangen, B. Šavija, Experimentally validated meso-scale fracture modelling of mortar using output from micromechanical models, Cem. Concr. Compos. 110 (2020), https://doi.org/10.1016/j.cemconcomp.2020.103567 103567.
[61] L.Y. Lv, H. Zhang, E. Schlangen, Z. Yang, F. Xing, Experimental and numerical study of crack behaviour for capsule-based self-healing cementitious materials, Constr. Build. Mater. 156 (2017) 219–229, https://doi.org/10.1016/j.conbuildmat.2017.08.157.
[62] H. Zhang, Y. Xu, Y. Gan, Z. Chang, E. Schlangen, B. Šavija, Microstructure informed micromechanical modelling of hydrated cement paste: techniques and challenges, Constr. Build. Mater. 251 (2020), https://doi.org/10.1016/j.conbuildmat.2020.118983 118983.
[63] Z Li, L Wamg, G Ma, Mechanical improvement of continuous steel microcable reinforced geopolymer composites for 3D printing subjected to different loading conditions, Composites Part B: Engineering 187 (2020), https://doi.org/10.1016/j.compositesb.2020.107796 107796.